Research Article | Vol. 28, No. 7 / 30 March 2020 / Optics Express 10386

Optics EXPRESS

Imaging through highly scattering environments using ballistic and quasi-ballistic light in a common-path Sagnac interferometer

JESSE DYKES,[1] ZEINA NAZER,[1] ALLARD P. MOSK,[2] AND OTTO L. MUSKENS[1,*]

[1] *Physics and Astronomy, Faculty of Engineering and Physical Sciences, University of Southampton, Southampton, UK*

[2] *Utrecht University, Debye Institute for Nanomaterials Science, The Netherlands*

[*] *o.muskens@soton.ac.uk*

Abstract: The survival of time-reversal symmetry in the presence of strong multiple scattering lies at the heart of some of the most robust interference effects of light in complex media. Here, the use of time-reversed light paths for imaging in highly scattering environments is investigated. A common-path Sagnac interferometer is constructed that is able to detect objects behind a layer of strongly scattering material at up to 14 mean free paths of total attenuation length. A spatial offset between the two light paths is used to suppress non-specific scattering contributions, limiting the signal to the volume of overlap. Scaling of the specific signal intensity indicates a transition from ballistic to quasi-ballistic contributions as the scattering thickness is increased. The characteristic frequency dependence for the coherent modulation signal provides a path length dependent signature, while the spatial overlap requirement allows for short-range 3D imaging. The technique of common-path, bistatic interferometry offers a conceptually novel approach that could open new applications in diverse areas such as medical imaging, machine vision, sensors, and lidar.

1. Introduction

The development of new methods capable of detecting objects on length scales from millimeters to hundreds of meters is of great importance for technology areas ranging from biomedical imaging to autonomous vehicle navigation. Commonly used methods include optical coherence tomography, time-of-flight and coherent lidar techniques [1,2]. Most imaging and ranging methods are strongly challenged in performance in situations of low visibility due to haze and scattering when dealing with environments such as biological tissue, rain, snow, fog, and clouds [2–4]. In such environments, the signal of interest is strongly attenuated while non-specific scattering backgrounds are greatly enhanced. Techniques that are robust against strong scattering are of interest to increase the visibility and hence improve safety, e.g. in autonomous vehicles.

In scattering environments, ballistic and quasi-ballistic components are often the only recoverable specific signatures, and efforts at extending the detection range of these components are of importance. In optical coherence tomography (OCT), recovery of ballistic signals is possible through many mean free paths while the imaging distances are generally on the millimeter scale [5,6]. On larger length scales, time-gated photon counting is another well-explored strategy, of particular interest for pulsed lidar [3,7,8]. Next to the recovery of weak ballistic components, detection and imaging of objects using the scattered light itself is seeing seen rapidly increasing interest [9–14]. While significant progress is being made to speed up reconstruction of scattered

#387503 https://doi.org/10.1364/OE.387503
Journal © 2020 Received 9 Jan 2020; revised 1 Mar 2020; accepted 2 Mar 2020; published 25 Mar 2020

Optics EXPRESS

information [15], in many dynamic scattering environments the decorrelation times are still too short for speckle-based reconstruction methods.

A specific class of methods for discriminating scattered and ballistic components involves bistatic techniques where illumination and detection paths are spatially separated to allow rejection of scattering. Spatially offset detection has been used particularly successfully in Raman detection through opaque media [16,17]. In OCT, the use of spatially offset, bistatic detection has been shown to provide an additional advantage for the selection of signals from deep inside scattering tissue [18,19]. In long-range bistatic lidar, similar principles of spatially offset excitation and detection paths are used to distinguish signals from different atmospheric regions [20]. These techniques have in common that only a single, unidirectional path from illumination to detection is used.

In this work, we propose and demonstrate a conceptually distinct approach to active detection of objects in scattering environments. Our approach is motivated by the guiding principle that time-reversed light paths produce some of the most robust interference effects in scattering media [21,22] and therefore these paths could be useful for detection and imaging of objects. An example of this idea is low-coherence enhanced backscattering spectroscopy, where interference of time-reversed light paths in backscattering is used for depth resolved biomedical imaging [23,24]. Time-reversal symmetry is also a prominent feature of the common-path Sagnac interferometer [25], which has found wide application in fiber optic gyroscopes [26,27]. We furthermore highlight the exceptional phase stability of common-path interferometers, with applications for example in metrology [28,29] and gravitational wave detection [30].

The basic idea here is that light going along a path and its time-reversed path accumulates the same phase, irrespective of how much scattering there was. Under these conditions of perfect symmetry a Sagnac-like interferometer would measure no specific target signal, but the symmetry is broken by an electro-optic modulator in one of the arms. This phase modulation allows to select with high precision the signal corresponding to the two beams that are being reflected from the same spot by a hidden object. The interference of light going through the two time-reversed paths in combination with electro-optic phase modulation provides a very specific signature which can be sensitively detected even after many scattering lengths. It is found that the scaling of target signal with attenuation length follows a less than exponential trend, indicating that the technique, next to providing the ballistic component, has a sensitivity to non-ballistic scattered light travelling in the same direction as the ballistic beam. The use of this signal for imaging and ranging is critically discussed.

2. Method

The experimental arrangement is shown in Fig. 1. The method makes use of a common-path Sagnac interferometer consisting of two counterpropagating light paths, where the target object forms part of the interferometer. A 1550 nm narrowband laser (Keysight) with a bandwidth of 500 kHz was amplified using a polarization maintaining Erbium-doped Fiber Amplifier (Pritel) to a total power of 400 mW. An optical isolator was used to protect the laser against backscattering from the setup. The output was split into two arms using a 75%:25% fiber optic splitter, of which the 25% port was sent to an electro-optic phase modulator (EOM, Jenoptik) and 75% was coupled out directly to free space. This unbalanced ratio of the splitter was chosen to reduce the power through the EOM to avoid damage to the component. Polarization-maintaining (PM) components were used throughout the fiber optic system, with angled (APC) fiber couplers to minimize spurious reflections. The two outputs were collimated using graded-index (GRIN) lensed fibers with specified return loss less than -60 dB (Oz Optics). Despite the use of fiber components with very low return loss, internal reflections still provided a significant background far above the detector noise floor. Therefore, an additional low-frequency (20 kHz) chopper in the free space path was included to reject spurious signals originating from the fiber optical system.

Optics EXPRESS

A half-wavelength ($\lambda/2$) waveplate was used to align the linear polarization states of the two outputs, which is a prerequisite for obtaining an interferometric signal. Additionally, a quarter waveplate was inserted in each of the arms to reduce backscattering into the same arm, exploiting the helicity nonconserving characteristics of single backscattering events. The use of circular polarized light reduced the noise floor by a factor three, mainly due to reduced backscattering from the mechanical chopper.

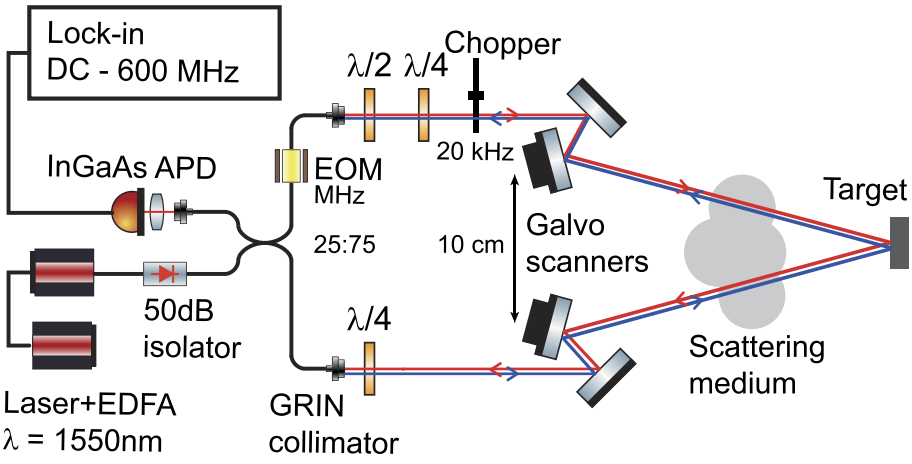

Fig. 1. Optical setup, including fiber optical system with laser at 1550 nm wavelength, erbium-doped fiber amplifier (EDFA), optical isolator, 75:25 splitter, electro-optic modulator (EOM), and graded-index (GRIN) collimators, and free-space optics with waveplates ($\lambda/2$, $\lambda/4$), optical chopper, galvo scanners and InGaAs avalanche photodetector (APD). Blue and red lines indicate the two counterpropagating light paths to the target and through the scattering medium (grey area).

The two collimated beams were directed to the target using a synchronized pair of 2D galvo scanners (Thorlabs GVS002), which were used for imaging at rates of 20,000 pixels per second as discussed below. After interaction with the target, backscattered light was collected using the same GRIN lenses and was sent through the fiber optical system in opposite direction where it was detected at the return port of the fiber splitter using an avalanche photodiode (APD, Thorlabs). The APD had a bandwidth of 400 MHz and noise equivalent power (NEP) of 0.3 pW/Hz$^{1/2}$. The frequency modulated components were extracted from the APD signal using a high-frequency lock-in amplifier (Zurich Instruments UHFLI) with an operating bandwidth of DC-600 MHz. The phase modulation resulted in a typical Fourier spectrum comprising of harmonics of the EOM driving frequency f. The highest modulation amplitude was obtained at the second harmonic of the driving frequency $2f$, rather than at the fundamental f. This property is useful as it allows us to avoid the residual amplitude modulation of the EOM occurring primarily at f. The lock-in bandwidth determines the coherence time used for averaging the phase-sensitive mixing signal. In our work the minimum coherence time was 50 μs which was limited by the 20 kHz mechanical chopper (at least one period is needed for signal extraction).

The fibres are single mode fibres with a 1/e mode field diameter of 7.1 μm and a numerial aperture (NA) of 0.12. In our imaging system, the fibre outputs are collimated to a 1/e beam waist w_0 of 0.64 mm. The corresponding diffraction limited divergence angle is $\theta = 0.77$ mrad. The resolution is given by the Rayleigh criterion as the separation of one diffraction limited beam waist, which at distance z, corresponds to $w(z) = w_0(1 + (z/z_R)^2)^{1/2}$ where $z_R = w_0/\theta = 0.8$ m is the Rayleigh length of the system. The vertical resolution is exactly $\Delta y = w(z)$, while the horizontal resolution is the projection of $w(z)$ onto the object at an angle $\phi/2$ with the normal,

Optics EXPRESS

i.e. $\Delta x = w(z)/\cos(\phi/2)$, where ϕ denotes the angle between the two beams in the bistatic setup. The axial resolution is given by the beam overlap for a given angle between the two beams, which is given by $\Delta z = w(z)/\tan(\phi)$. In our setup, $\phi = 10^\circ$ giving a resolution of $\Delta x = 1.29$ mm, $\Delta y = 1.28$ mm and $\Delta z = 7.26$ mm.

The galvo scanners were controlled by two Red Pitaya STEMlab modules which were set up as dual channel function generators providing synchronized sweeps. One of the Pitayas controlled the X axes at 100 Hz line rate, while the other controlled the Y axes of the galvos using a slower, 0.5 Hz ramp. Independent offsets and scale factors were introduced for each of the channels to account for small differences in the calibration of the scanners. These corrections resulted in a good beam overlap over the entire scan field. A Labview program was used to start and stop the sweeps. Images were collected directly through the UHLFI lock-in amplifier by using the Data Acquisition advanced triggering tool.

3. Frequency dependence of common-path signal

The mixing of scattered fields collected from the two counterpropagating light paths provided a phase stable interferometric signal under the condition that the system is stable during the roundtrip time and is not rotating. The EOM breaks the symmetry by introducing a time-varying phase $\phi(t) = \phi_0/2\sin(2\pi ft)$, where ϕ_0 denotes the peak to peak amplitude of modulation and f is the EOM driving frequency. Light travelling through the two counterpropagating light paths arrives at the EOM from opposite sides, separated by a time delay τ. The mixing of these two scattered field components results in a heterodyne mixing signal $S(t) = E_{\mathrm{CW}}E^*_{\mathrm{CCW}} = |E|^2\exp[i(\phi(t+\tau)-\phi(t))]$ where $|E|$ denotes the amplitude of the two scattered fields in clockwise (CW) and counter-clockwise (CCW) directions, which are taken to be equal by symmetry. The derivation of the power spectrum from the phase-modulated signal follows standard trigonometric manipulations similar to diffraction by sinusoidal phase gratings [31–33]. After expansion of terms $\exp[i\phi_0\sin(2\pi ft)/2] = \sum_{q=-\infty}^{\infty} J_q(\phi_0/2)\exp[i2\pi qft]$, where $J_q(z)$ are Bessel functions of the first kind, and following a Fourier transform, the heterodyne mixing signal is obtained as

$$S(\omega) = \frac{|E|^2}{2\pi}\sum_{q,p=-\infty}^{\infty} J_q(\phi_0/2)J_p(\phi_0/2)\exp\left(i2\pi qf\tau\right)\delta[\omega - 2\pi(q-p)f]\,. \tag{1}$$

Identifying $n = q - p$ as the harmonic of the frequency spectrum defined by the Dirac delta function, we obtain an expression for the n-th harmonic components, S_n, according to

$$S_n = \frac{|E|^2}{2\pi}\sum_{q=-\infty}^{\infty} J_q(\phi_0/2)J_{q-n}(\phi_0/2)\exp\left(i2\pi qf\tau\right). \tag{2}$$

The modulus of each harmonic is then obtained through the spectral power, $P_n = |S_n|^2$, which follows as

$$\begin{aligned} P_n = \frac{|E|^4}{4\pi^2}\sum_{q,r=-\infty}^{\infty} & J_q(\phi_0/2)J_{q-n}(\phi_0/2) \\ & \times J_r(\phi_0/2)J_{r-n}(\phi_0/2)\cos[2\pi f\tau(q-r)]\,. \end{aligned} \tag{3}$$

Figure 2(a) shows experimental frequency sweeps of the modulus of the second harmonic signal intensity $|S_2| = (P_2)^{1/2}$ for four different values of the EOM driving voltage. Fits to the data are given in Fig. 2(b) and show good agreement with the general behaviour for values of ϕ_0 in the range 0.3π to 1.5π. For the fits we truncated the summations over q, r from -10 to +10, providing convergence of the result to 0.001%. The extraction of the modulated signal using the lock-in amplifier was done using a two-stage scheme where the output of the signal at the harmonic of the EOM drive frequency f was measured with a short (4 μs) integration time, and subsequently

Optics EXPRESS

the modulus of this signal was used as the input for the second lock-in stage operating at the chopper frequency f_{chop}. This method was suitable for the lock-in amplifier to track the EOM frequency sweep. Alternatively, direct detection at the sum frequency of the EOM and chopper was possible for a fixed modulation frequency. From the expression for $S(t)$ we immediately identify that for $\phi(t+\tau) = \phi(t)$, the phases are the same and modulated signal is zero. This condition is fulfilled for frequencies equal to an integer multiple n of the inverse of the roundtrip time, $f = n/\tau$. From the zeros in the frequency sweep, we find a roundtrip distance of 4.5 m, which includes approximately 2 m length of fiber from the EOM to the GRIN output coupler and 1 m of roundtrip distance to the target.

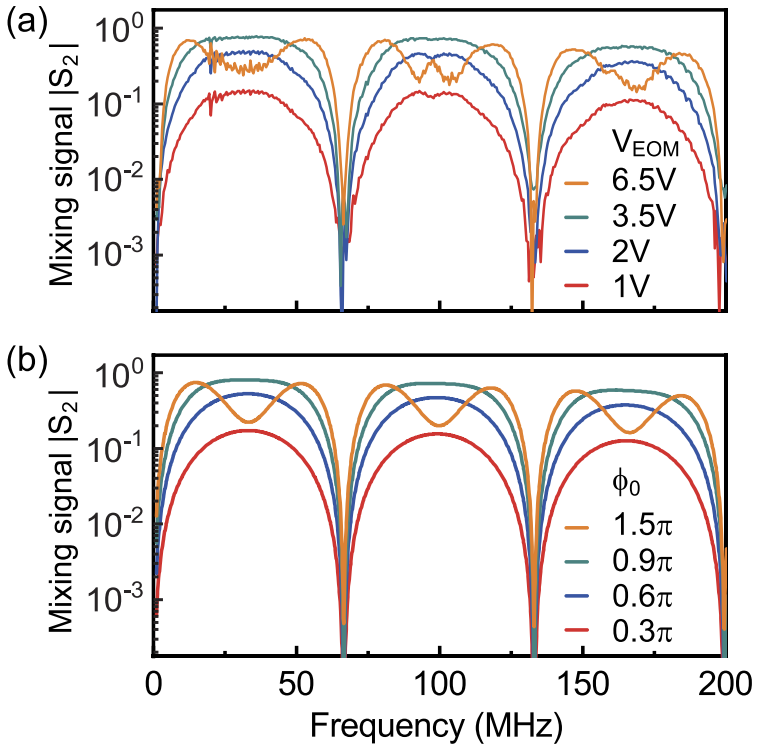

Fig. 2. Measured (a) and calculated (b) modulus of the mixing signal $|S_2|$ at $2f$ against driving frequency f, for a fixed roundtrip time $\tau = 5$ ns, corresponding to 1.5 m path length. Different values of the EOM driving voltage correspond to different peak-to-peak phase amplitudes ϕ_0, shown by calculated curves in (b).

4. Object detection and imaging through scattering media

To investigate the attenuation of the target signal after propagation through a scattering medium, we measured the signal after propagation through a stack of sheets of Polytetrafluoroethylene (PTFE, Teflon), where each sheet was 0.5 mm thick. The weakly scattering PTFE is considered a reasonable approximation for light scattering in biological tissue, while it is a simplification for environmental scattering media like clouds and fog which are otherwise considerably more difficult to model in a laboratory environment. The characterization of the scattering medium is presented in the Appendix. Using ballistic and total transmission measurements we obtained a scattering mean free path at 1550 nm wavelength of $l_s = 0.36 \pm 0.02$ mm, a transport mean free path $\ell = 0.50 \pm 0.03$ mm, and a diffuse absorption length $L_a = 10 \pm 1$ mm for PTFE. Each slab

Optics EXPRESS

therefore represents a total attenuation length in reflection (i.e. double pass) of $2L/l_s = 2.8$. Our values of the scattering length are three times larger than values reported at 800 nm wavelength for the same material [34], which is consistent with the expected wavelength scaling.

The target signal intensity was measured for increasing thicknesses of the scattering PTFE stack of up to 6 slabs ($2L/l_s = 16.8$). Figure 3 shows the mixing signal intensity against scattering length using a mirror as a target with high specular reflectivity (diamonds, blue). The mirror target was placed at a distance of 50 cm from the galvo scanners. For the cases of zero and one PTFE slab, additional neutral density filters were used to attenuate the signal. All values are normalized to the return signal obtained without scattering medium. It is expected that the mixing signal $|S_2|$ should follow an exponential decay proportional to the Beer-Lambert law $|S(2)| = \exp(-2L/l_s)$. This is a direct consequence of the exact symmetry of the two (direct and time-reversed) propagators through the scattering medium. The Beer-Lambert scaling is indicated by the solid blue curve.

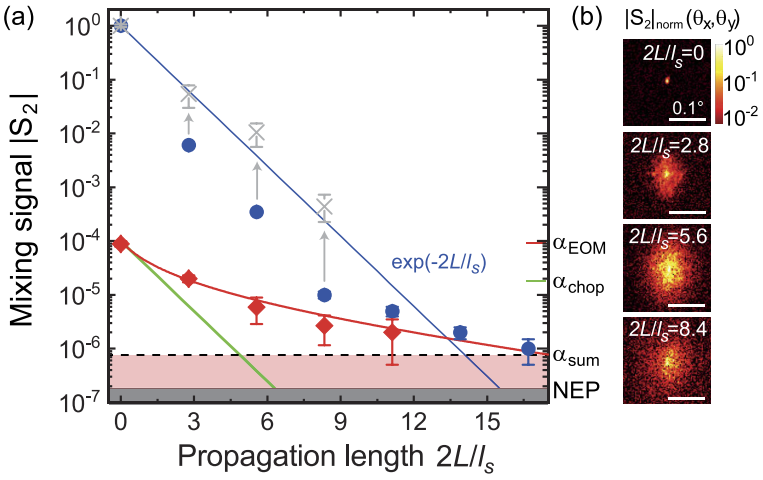

Fig. 3. Dependence of reflection signal intensity $|S_2|$ on total attenuation length $2L/l_s$, for the specular reflection from a protected silver mirror (dots, blue) and diffuse reflector (diamonds, red, DG10-220, Thorlabs). Blue and red lines indicate exponential decay using Beer-Lambert law $|S_2| \propto \exp(-2L/l_s)$. Lines on right indicated background (noise) levels for EOM only at $2f$ (α_{EOM}) and chopper only at f_{chop} (α_{chop} modulation, as well as sum frequency detection at $2f + f_{\mathrm{chop}}$ (α_{sum}), with NEP indicating the detector noise floor. (b) Angular θ_x, θ_y scans (log-scale) of the target showing angular spread of detection signal for attenuation lengths of 0, 2.8, and 5.6 mean free paths. Grey crosses in (a) indicate ballistic intensity corrected for angular spreading calculated using angular scans from (b).

However, the experimental signal drops faster than the expected attenuation. The additional drop in signal is attributed to an angular spreading of the ballistic beam due to beam distortions caused by the scattering slabs. The combination of surface roughness (and possibly some near-forward bulk scattering) of the stack of PTFE slabs distorts the beam profile of the ballistic beam, resulting in an angular spreading of the beam from the original diffraction-limited beam with $\theta \simeq 0.044°$ (0.77 mrad) to $> 0.1°$. The angular broadening is clearly seen in angular scans of the signal $|S_2|(\theta_x, \theta_y)$, as presented in Fig. 3(b). The maps are normalized and are shown on logarithmic scale. Angular broadening larger than the collection angle results in a reduced peak intensity, and hence a drop in signal below the expected attenuation $|S_2| = \exp(-2L/l_s)$ as indicated by the blue line. It is possible to estimate the original amplitude of the ballistic signal by integrating $|S_2|$ over the angular cone and normalizing to the acceptance angle, which resulted in values indicated by the grey crosses in Fig. 3(a). Here the vertical errors relate to an

Optics EXPRESS

uncertainty in the integration boundary of the ballistic component because of the non-ballistic scattering background. We see that the observed trend is consistent with Beer-Lambert's law when correcting for the angular spreading of the ballistic beam. Exponential attenuation was also observed in ballistic transmission experiments, which were collected over a larger aperture of 0.6° as is presented in the Appendix.

For attenuation lengths above 8 mean free paths, we see a different slope and eventually the predicted exponential attenuation even crosses below the measured signal level at $2L/l_s = 14$. The different slope indicates that the setup is able to recover some of the non-ballistic light that is produced by the surface roughness and bulk scattering and which travels in the same direction as the ballistic beam. A discernible signal could be detected at up to 14 mean free paths of total attenuation length. This detection limit corresponds to a sensitivity of 6 orders of magnitude in the mixing signal $|S_2|$.

The non-ballistic origin of the signal is also seen when replacing the specular mirror target by a diffuse reflector (Thorlabs DG10-220), resulting in the signal indicated by the red dots in Fig. 3. Without the scattering medium, the diffuse target already resulted in four orders less signal intensity than the specular target. The attenuation of intensity with increasing scattering length is much less steep than the expected exponential (Beer-Lambert) law for ballistic components, suggeting that double small-angle scattering events occur that add to the coherently detected signal. We emphasize that the detection of the non-ballistic component is nontrivial as it involves a phase stable heterodyne mixing signal, which is provided by the time-reversal symmetry of light travelling in both directions through the quasi-ballistic light paths. This property renders the common-path technique more robust against scattering than other coherent detection schemes.

The figure also shows the detection limits for different modulation schemes. In particular we compare the noise floor for detection using only the EOM modulation, indicated by α_{EOM}, and only the chopper modulation, indicated by α_{chop}. As discussed in the methods section, the EOM modulation by itself results in a spurious background signal caused by internal reflections in the fiber at a level of $\alpha_{\mathrm{EOM}} = 10^{-4}$ in the mixing signal $|S_2|$ taken at $2f$. Detection using only the mechanical chopper and no EOM, results in high levels of low-frequency (kHz) instrumental noise at a level $\alpha_{\mathrm{chop}} = 2 \times 10^{-5}$. The combined modulation scheme at the sum of the EOM and chopper frequencies, or equivalently using a two-stage cascaded lock-in detection at $2f$ and f_{chop} respectively, is substantially lower and is found to be ultimately limited by backscattering from the chopper in our setup to a level $\alpha_{\mathrm{sum}} = 8 \times 10^{-7}$. The sensitivity limit of the APD noise equivalent power (NEP) is yet a factor of five lower than α_{sum} and might be attainable through further improvements in the setup. We note that an additional order of magnitude sensitivity could be gained at the high intensity end of the curve, by placing ×3 beam expanders in the arms which reduces the diffraction of the beams and hence improves the overall system throughput for a specular reflector. However this only affected the throughput of the collimated beam in absence of scattering (i.e. the highest detected intensity), whereas the lowest signals were limited by the total étendue (angle times area) of the system which is unaltered by the beam expansion.

In comparison, OCT is capable of imaging at $2L = 12l_s$ for given signal to noise (SNR) of 10^{-5} [14]. In comparison, our system shows a noise floor of 10^{-6} of the signal without scattering. On the basis of SNR alone therefore we estimate that our detection limit should be around $14l_s$. This could potentially be further extended to $16l_s$ by suppressing spurious backscattering noise in the setup to reach the NEP of the detector at SNR 10^{-7}.

The presence of a specific signal from the target in the common-path interferometer can be used for imaging through the scattering medium as shown in Fig. 4. In this experiment, the scattering medium was placed 50 mm in front of the target to ensure a sufficiently large separation compared to the imaging depth Δz. Figure 4(a) illustrates this layout, which shows the position of the scattering medium at around $z = 30$ mm and the target at $z = 80$ mm. Images were taken at different depths z, which could be done either by translating the scene (target plus scattering

Optics EXPRESS

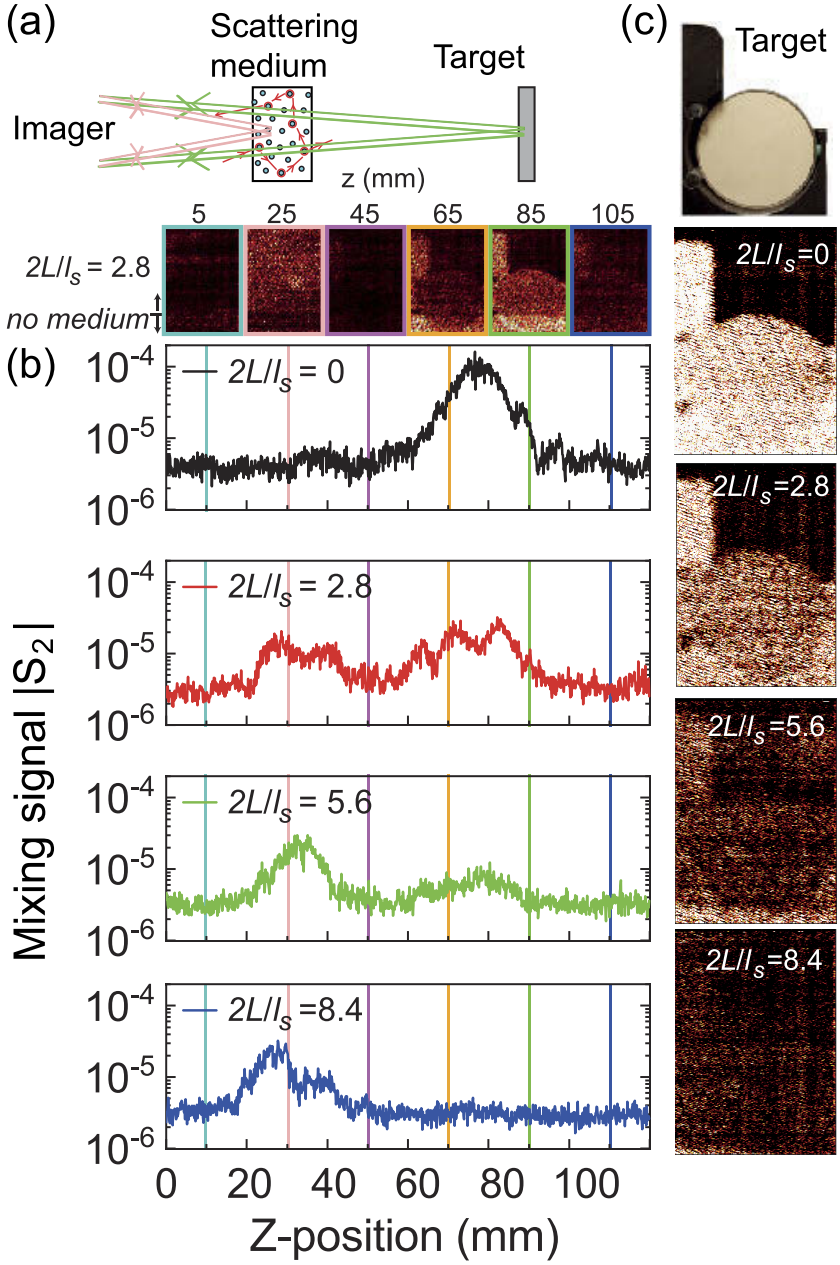

Fig. 4. (a) Images taken at different positions z, showing position of scattering medium and target diffuse reflector. Top part of image was covered by scattering medium with $2L/l_s = 2.8$, bottom part without scattering medium. (b) Dependence of mixing signal intensity $|S_2|$ (log-scale) versus position z for different attenuation lengths from 0 to 8.4 mean free paths. (c) Image of target at $z = 75$ mm for attenuation lengths corresponding to (b).

Optics EXPRESS

medium) or by adjusting the galvo mirrors to change the overlap in z, both resulting in the same response. Images collected at different depths z are shown in Fig. 4(a) for a single slab of teflon ($2L/l_s = 2.8$). The bottom part of the image was not covered by the slab, hence showing the signal without scattering medium. The target is located at $z = 80$ mm and the images reveal a depth of view of ±10 mm around this position. Figure 4(b) shows the collected peak intensity in the centre of the image while the z-position was scanned. For increasing amounts of attenuation $2L/l_s$, the target signal intensity decreases. The addition of the scattering medium results in a new signal located at around $z = 30$ mm, corresponding to the position of the slabs. Increasing numbers of slabs were loaded at the front of the stack, resulting in an overall shift of the front of the scattering medium to smaller z by 0.5 mm per slab. For attenuation over 5.6 scattering lengths, the scattering of the medium overwhelms the target response, however the latter can still be distinguished because of the spatial offset of the two signals. The spatial offset of the two light paths results in an effective rejection of scattering from the individual arms, and signals are only observed from the volume in which the two beams are overlapping.

5. Potential for 3D imaging and ranging

To demonstrate the capability of extracting three-dimensional object information, we performed measurements without scattering layer, using a test object shown in Fig. 5(a). The object, a wooden chess piece, was imaged using the common-path interferometer at three different positions z. A composite image is shown in Fig. 5(b) was generated by encoding the different images into three colors blue, red and yellow, while the individual images are shown in Fig. 5(c). Images taken at a separation of 5 mm in depth show different parts of the structure and reveal the three dimensional nature of the object. The depth of view is determined by the angle between the

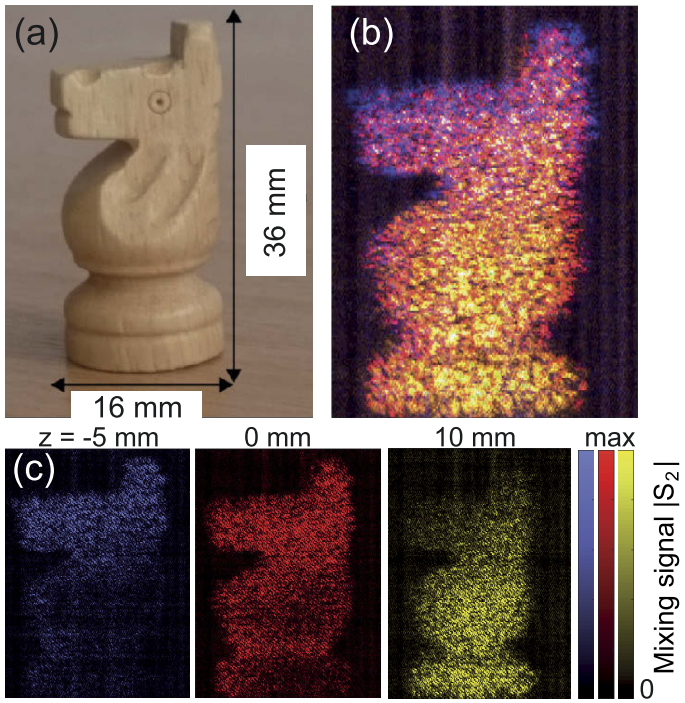

Fig. 5. (a) Photograph of chess piece used in experiment. (b) Composite image of 3D chess piece using color channels blue, red, yellow for three distances. (c) corresponding images taken at relative positions $z = -5$ mm, 0 mm and 10 mm.

Optics EXPRESS

two incident beams, which amounted to 10° in our study. Steeper incidence can be obtained by increasing the separation of the two galvo mirror scanners, or by reducing the object distance. The composite image clearly shows a grainy structure representing individual angular speckles of the light scattered from the object back into the aperture of the fiber optic system.

The direct relation between the roundtrip time and the zeros in the response against driving frequency could be of interest for applications in ranging. This relation is explored in Eq. (3) and Fig. 2 for a phase stable signal from a perfect mirror and it is important to assess the robustness of this signature in the presence of scattering. Figure 6(a) shows the frequency sweeps taken for the mirror target in presence of scattering medium of up to $2L/l_s = 8.4$ total attenuation length. While the signature is retained for weak scattering up to 2.8 attenuation lengths, the characteristic frequency dependence is absent for strongly scattering environments. We found in Fig. 3 that in this regime the ballistic beam is already distorted by surface roughness and near-forward scattering, and the angular profiles showed a grainy speckle structure. The frequency spectrum in Fig. 6(a) shows a rapid variation of intensities which can be interpreted as speckle. Indeed a histogram of the intensities taken over 10,000 points shown in Fig. 6(b) shows a characteristic exponential Rayleigh statistics, where the line represents the Rayleigh probability distribution for a speckle contrast of 75%. Thus, the detected signal, while phase stable, shows a fast intensity modulation due to the dynamics of the speckle field. An identical behaviour was found for the diffuse reflector in absence of scattering medium (not shown here). We therefore speculate

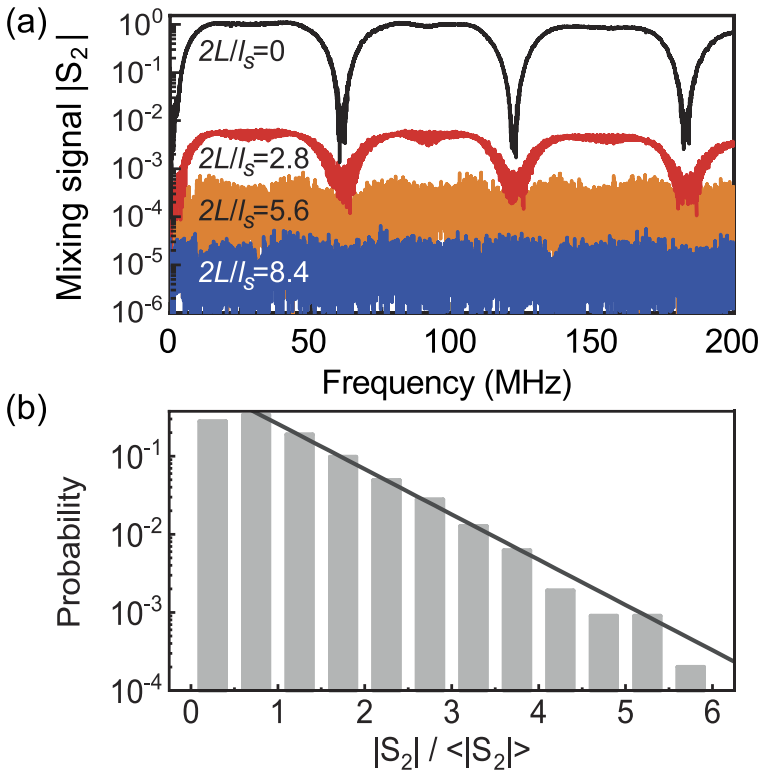

Fig. 6. (a) Frequency sweeps of signal from a mirror reflector, for different attenuation lengths, showing loss of characteristic modulation signature in presence of strong multiple scattering. (b) Probability histogram of 10,000 measurements taken for the $2L/l_s = 8.4$ attenuation lengths and normalized to the ensemble average $\langle|S_2|\rangle$, with black line showing Rayleigh statistics for a speckle contrast of 75%.

Optics EXPRESS

that the increased role of phase fluctuations in the near-forward speckle is responsible for the flattening of the frequency response and disappearance of the characteristic zeros for return signals $|S_2|$ below 10^{-4} of the signal of the reference mirror. Therefore long-distance ranging using this method appears possible for well defined reflection signals from specular targets, but is easily compromised in the presence of scattering or speckle produced by beam distortions or diffuse target reflections.

One of the main differences of our common path approach with conventional heterodyne interferometry is the lack of a local reference field. Common path interferometry offers as a key advantage a reduced sensitivity of the mixing signal to disturbances such as turbulence and scattering. A clear disadvantage of this approach is the lack of detection gain, which is usually achieved by mixing with a local oscillator, and therefore the signal strength drops off steeply as the square of the scattered field. Another important aspect is that, in common-path interferometry, both light fields are reflected from the same target, therefore the common path interferometer will exhibit no Doppler beat signal for moving targets. A Doppler-free signal at a well defined modulation frequency can offer advantages related to the highly stable lock-in detection for extracting signals. However the lack of Doppler information poses limitations in applications such as lidar. We speculate that it may be possible to combine common-path interferometry with other coherent modulation schemes such as frequency modulated continuous wave (FMCW) sweeps, through sweeping of the EOM frequency, which could be explored in future studies.

6. Conclusion

In conclusion, we have developed an imaging system making use of time-reversed light paths in a common-path configuration to detect objects. The properties of the technique include spatially-offset beams for rejection of single scattering, electro-optic modulation for phase-sensitive detection of the time-reversal interference, and a distant dependent ruler. We successfully demonstrate imaging of targets through a scattering medium with total attenuation lengths of up to 14 mean free paths, which can likely be further increased by improvements in instrumentation. We expect that elements of the technique will be of interest in a variety of applications in object detection and imaging, potentially including medical imaging, machine vision, sensors, and lidar. Our results invite future studies which could explore the windows of opportunity of this approach in these specific applications.

Appendix

Characterization of teflon scattering at 1550 nm

The optical scattering parameters of teflon at 1550 nm wavelength were studied using a combination of ballistic beam transmission and diffuse total transmission experiments. Figure 7 shows the optical transmission through stacks of Teflon slabs, for both the ballistic component and the total transmission. The ballistic light was measured through a 1 cm diameter iris positioned at a distance of 1 m from the scattering medium, therefore collecting light transmitted within an angle of 0.6° from the forward direction. Total transmission was measured using an integrating sphere.

For a thick medium, total transmission is determined by the diffuse scattering component given by the relation $T_{\mathrm{tot}} = (1 + \tau_e)/(L/l_t + 2\tau_e) \exp(-L/L_{\mathrm{abs}})$. Here, τ_e is the extrapolation factor which contains internal reflection due to the index mismatch and which is close to 1 for the refractive index of teflon. Absorption is included through the diffuse absorption length which in diffusion approximation is defined as $L_{\mathrm{abs}} = (l_t l_a/3)^{1/2}$. Here l_a is the bulk absorption length. A model fit using this equation (blue line in Fig. 7) gives a transport mean free path of 0.50 ± 0.03 mm and a diffuse absorption length of 10 ± 1 mm. Thus absorption is quite low for the experimental conditions of this work.

Optics EXPRESS

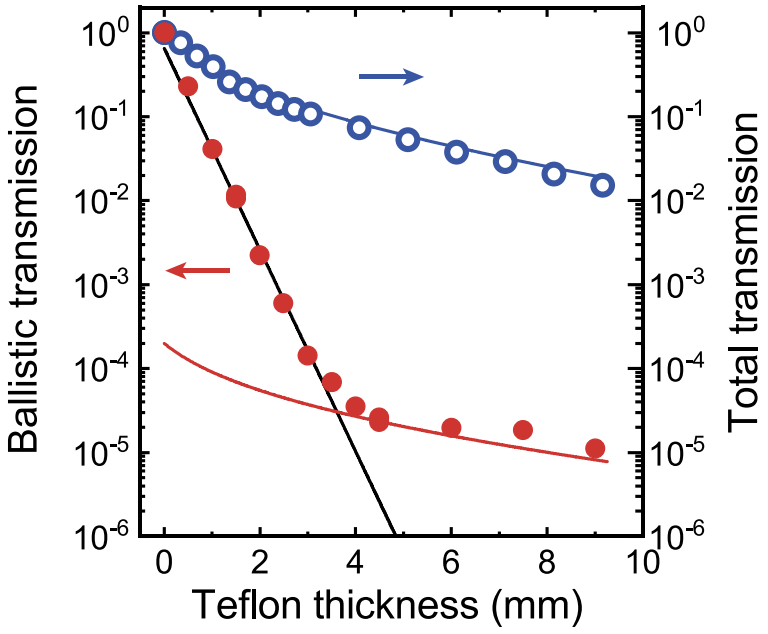

Fig. 7. Ballistic transmission (red dots) and total transmission (blue open circles) through stacks of teflon slabs of increasing total thickness. Lines are fits using Beer-Lambert equation $I/I_0 = \exp(-L/l_s)$ (black) and total transmission $T_{\text{tot}} = (1+\tau_e)/(L/l_t + 2\tau_e)\exp(-L/L_{\text{abs}})$ (blue). Red line is total transmission scaled by factor 2×10^{-4}.

The ballistic transmission (red dots in Fig. 7) shows an exponential decay with the slab thickness up to about 4 mm with a scattering length of 0.36 ± 0.01 mm. The difference between the scattering and transport mean free paths indicates that scattering is not completely isotropic, and it takes approximately 1.5 scattering lengths to completely average over all angles. After 4 mm the slope is reduced, indicative that the diffuse scattering component dominates the transmission in the selected aperture for larger thickness. This thickness corresponds to about 10 scattering mean free paths. The red line corresponds to a fraction of the diffuse total transmission corresponding to the ratio of detected scattering solid angle (3×10^{-4} sr) to the hemispheric total transmission.

Funding

Defence Science and Technology Laboratory (DSTLX-1000108034, DSTLX-1000127842); Engineering and Physical Sciences Research Council (EP/J016918/1); Nederlandse Organisatie voor Wetenschappelijk Onderzoek (NWO) (68047618).

Acknowledgments

The authors would like to thank Xiaoqing Xu for his help in the initial phase of the experiment. OM acknowledges support by the University of Utrecht through the Debye Chair visiting professorship. All data supporting this study are openly available from the University of Southampton repository (DOI: 10.5258/SOTON/D1262).

Disclosures

The authors declare no conflicts of interest.

Optics EXPRESS

References

1. G. Berkovic and E. Shafir, "Optical methods for distance and displacement measurements," Adv. Opt. Photonics **4**(4), 441–471 (2012).
2. C. Dunsby and P. M. W. French, "Techniques for depth-resolved imaging through turbid media including coherence-gated imaging," J. Phys. D: Appl. Phys. **36**(14), R207–R227 (2003).
3. R. Tobin, A. Halimi, A. McCarthy, M. Laurenzis, F. Christnacher, and G. S. Buller, "Three-dimensional single-photon imaging through obscurants," Opt. Express **27**(4), 4590–4611 (2019).
4. P. Feneyrou, L. Leviandier, J. Minet, G. Pillet, A. Martin, D. Dolfi, J.-P. Schlotterbeck, P. Rondeau, X. Lacondemine, A. Rieu, and T. Midavaine, "Frequency-modulated multifunction LiDAR for anemometry, range finding, and velocimetry-1. Theory and signal processing," Appl. Opt. **56**(35), 9663–9675 (2017).
5. A. F. Fercher, W. Drexler, C. K. Hitzenberger, and T. Lasser, "Optical coherence tomography - principles and applications," Rep. Prog. Phys. **66**(2), 239–303 (2003).
6. V. Duc Nguyen, D. J. Faber, E. Van Der Pol, T. G. Van Leeuwen, and J. Kalkman, "Dependent and multiple scattering in transmission and backscattering optical coherence tomography," Opt. Express **21**(24), 29145–29156 (2013).
7. K. Yoo and R. R. Alfano, "Time-resolved coherent and incoherent components of forward light scattering in random media," Opt. Lett. **15**(6), 320–322 (1990).
8. L. Wang, P. Ho, C. Liu, G. Zhang, and R. Alfano, "Ballistic 2-d imaging through scattering walls using an ultrafast optical Kerr gate," Science **253**(5021), 769–771 (1991).
9. Z. Yaqoob, D. Psaltis, M. S. Feld, and C. Yang, "Optical phase conjugation for turbidity suppression in biological samples," Nat. Photonics **2**(2), 110–115 (2008).
10. S. Popoff, G. Lerosey, R. Carminati, M. Fink, A. Boccara, and S. Gigan, "Measuring the transmission matrix in optics: An approach to the study and control of light propagation in disordered media," Phys. Rev. Lett. **104**(10), 100601 (2010).
11. J. Bertolotti, E. G. van Putten, C. Blum, A. Lagendijk, W. L. Vos, and A. P. Mosk, "Non-invasive imaging through opaque scattering layers," Nature **491**(7423), 232–234 (2012).
12. O. Katz, E. Small, and Y. Silberberg, "Looking around corners and through thin turbid layers in real time with scattered incoherent light," Nat. Photonics **6**(8), 549–553 (2012).
13. A. V. Kanaev, A. T. Watnik, D. F. Gardner, C. Metzler, K. P. Judd, P. Lebow, K. M. Novak, and J. R. Lindle, "Imaging through extreme scattering in extended dynamic media," Opt. Lett. **43**(13), 3088–3091 (2018).
14. A. Badon, D. Li, G. Lerosey, A. C. Boccara, M. Fink, and A. Aubry, "Smart optical coherence tomography for ultra-deep imaging through highly scattering media," Sci. Adv. **2**(11), e1600370 (2016).
15. O. Tzang, E. Niv, S. Singh, S. Labouesse, G. Myatt, and R. Piestun, "Wavefront shaping in complex media with a 350 kHz modulator via a 1D-to-2D transform," Nat. Photonics **13**(11), 788–793 (2019).
16. P. Matousek, I. P. Clark, E. R. C. Draper, M. D. Morris, A. E. Goodship N. Everall, M. Towrie, W. F. Finney, and A. W. Parker, "Subsurface probing in diffusely scattering media using spatially offset Raman spectroscopy," Appl. Spectrosc. **59**(4), 393–400 (2005).
17. M. Chen, J. Mas, L. H. Forbes, M. R. Andrews, and K. Dholakia, "Depth-resolved multimodal imaging: Wavelength modulated spatially offset Raman spectroscopy with optical coherence tomography," J. Biophotonics **11**(1), e201700129 (2018).
18. T. E. Matthews, M. Medina, J. R. Maher, H. Levinson, W. J. Brown, and A. Wax, "Deep tissue imaging using spectroscopic analysis of multiply scattered light," Optica **1**(2), 105–111 (2014).
19. Y. Zhao, W. J. Eldridge, J. R. Maher, S. Kim, M. Crose, M. Ibrahim, H. Levinson, and A. Wax, "Dual-axis optical coherence tomography for deep tissue imaging," Opt. Lett. **42**(12), 2302–2305 (2017).
20. J. E. Barnes, N. C. P. Sharma, and T. B. Kaplan, "Atmospheric aerosol profiling with a bistatic imaging lidar system," Appl. Opt. **46**(15), 2922–2929 (2007).
21. M. P. Van Albada and A. Lagendijk, "Observation of Weak Localization of Light in a Random Medium," Phys. Rev. Lett. **55**(24), 2692–2695 (1985).
22. P.-E. Wolf and G. Maret, "Weak Localization and Coherent Backscattering of Photons in Disordered Media," Phys. Rev. Lett. **55**(24), 2696–2699 (1985).
23. N. N. Boustany, S. A. Boppart, and V. Backman, "Microscopic Imaging and Spectroscopy with Scattered Light," Annu. Rev. Biomed. Eng. **12**(1), 285–314 (2010).
24. Y. L. Kim, Y. Liu, V. M. Turzhitsky, H. K. Roy, R. K. Wali, H. Subramanian, P. Pradhan, and V. Backman, "Low-coherence enhanced backscattering: review of principles and applications for colon cancer screening," J. Biomed. Opt. **11**(4), 041125 (2006).
25. G. Sagnac, "L'éther lumineux démontré par l'effet du vent relatif d'éther dans un interféromètre en rotation uniforme," C. R. Hebd. Seances Acad. Sci. **157**, 708–710 (1913).
26. V. Vali and R. W. Shorthill, "Fiber Ring Interferometer," Appl. Opt. **15**(5), 1099–1100 (1976).
27. W. W. Chow, J. Gea-Banacloche, L. M. Pedrotti, V. E. Sanders, W. Schleich, and M. O. Scully, "The ring laser gyro," Rev. Mod. Phys. **57**(1), 61–104 (1985).
28. D. H. Hurley and O. B. Wright, "Detection of ultrafast phenomena by use of a modified Sagnac interferometer," Opt. Lett. **24**(18), 1305–1307 (1999).
29. Y. Sugawara, O. B. Wright, O. Matsuda, M. Takigahira, Y. Tanaka, S. Tamura, and V. E. Gusev, "Watching ripples on crystals," Phys. Rev. Lett. **88**(18), 185504 (2002).

Optics EXPRESS

30. K.-X. Sun, M. M. Fejer, E. Gustafson, and R. L. Byer, "Sagnac Interferometer for Gravitational-Wave Detection," Phys. Rev. Lett. **76**(17), 3053–3056 (1996).
31. T. L. Beach and R. V. E. Lovelace, "Diffraction by a sinusoidal phase screen," Radio Sci. **32**(3), 913–921 (1997).
32. R. A. Bergh, H. C. Lefevre, and H. J. Shaw, "All-single-mode fiber-optic gyroscope with long-term stability," Opt. Lett. **6**(10), 502–504 (1981).
33. G. B. Malykin and E. G. Malykin, "On Possibility of Using the Lowest Odd Harmonics of the Phase Modulation Frequency in the Output Signal of the Fiber-Optic Ring Interferometer for Detection of the Sagnac Effect," Opt. Spectrosc. **105**(1), 117–123 (2008).
34. D. S. Wiersma, A. Muzzi, M. Colocci, and R. Righini, "Time-resolved experiments on light diffusion in anisotropic random media," Phys. Rev. E **62**(5), 6681–6687 (2000).